An instrument for studying the response of STACEE camera components to different lighting conditions

Pascal Fortin
Department of Physics
McGill University
Montreal, Quebec
Canada

February, 2000

A thesis submitted to the
Faculty of Graduate Studies and Research
in partial fulfillment of
the requirements for the degree of
Master of Science

Abstract

This thesis describes a new instrument used to study the response of the STACEE camera to different lighting conditions. It explains how the camera functions, and presents the results of different tests performed on the camera.

Résumé

Cette thèse décrit un nouvel instrument utilisé pour étudier la réponse de la caméra utilisée par l'expérience STACEE à différentes conditions d'éclairage. Elle explique le fonctionnement de la camera et présente les résultats des différents tests effectués sur la caméra.

Acknowledgements

I would like to thank my supervisors Ken Ragan and David Hanna for giving me the opportunity to join an exciting new experiment in the field of astroparticle physics. Thanks also to Claude Théoret for his precious help with PAW, and for all the discussions.

I am extremely grateful to my parents and sister, who always supported and encouraged me. Last but not least, I would like to thank Martine Bertrand for being by my side during all the good and bad moments. Many thanks.

Contents

List of Figures

Chapter 1

Introduction

The Solar Tower Atmospheric Cherenkov Effect Experiment (STACEE) is a new experiment in the field of high energy astrophysics. The interest for this field has literally exploded with the launch of the EGRET space telescope on board the Compton Gamma Ray Observatory. EGRET started its observing program on May 16, 1991, and operated at nominal efficiency for the following four years. The energy range covered by EGRET was 20 MeV to ~30 GeV, and the majority of the photons detected had energies near 100 MeV. A major discovery of EGRET has been the detection of more than 60 Active Galactic Nuclei (AGN) of the blazar class. The general model of blazars is one of a supermassive black hole surrounded by an accretion disk. A truly remarkable feature of blazars is their tremendous energy output. The apparent gamma ray luminosities derived from the measured fluxes and the known redshifts are as much as 10^{49} ergs sec^{-1}. The blazars detected by EGRET exhibited

intense and hard powerlaw spectra that generally continued without spectral breaks to 5 GeV. The observed spectra supported the possibility that blazars could be detected at very high energies. In fact, two such blazars, Markarian 421 and 501, have been detected at TeV energies by the Whipple Observatory and others [1–4].

The fact that many EGRET-detected AGN are not seen at TeV energies may signal cutoffs in the acceleration mechanism or absorption by soft photons either local to the source or in intergalactic space. The discovery of numerous gamma-ray emitting AGN at energies below 20 GeV highlights the need to extend observations on a large sample of AGN to higher energies. No telescope has operated in the energy region between 20 and 250 GeV, and next generation atmospheric Cherenkov detectors, such as STACEE, should explore this region in the next decade.

Direct detection of gamma rays can be done in space, but the atmosphere makes it impossible from the ground. At high energies only indirect gamma ray detection is possible. These high energy gamma rays initiate extensive air showers of particles which propagate down through the atmosphere. The high energy of the incident photon leads to shower particles at relativistic energies. The relativistic charged particles move faster than the speed of light in air and emit Cherenkov radiation. The Cherenkov photons are strongly beamed in the forward direction and they preserve the directional information contained in the shower particles. The Cherenkov radiation arrives at the ground with a tight time structure ($\sim$5 ns) permitting its detection by fast

Figure 1.1: NSTTF site at Sandia National Laboratories.

photosensitive detectors amidst the night sky light.

To first order, the energy threshold of an atmospheric Cherenkov telescope is limited by night sky fluctuations and scales inversely with the square root of the telescope mirror area. To get the threshold down to 20 GeV, the STACEE collaboration is using the existing array of heliostats of the National Solar Thermal Test Facility (NSTTF) at Sandia National Laboratories built for solar power study and generation. Figure 1.1 shows a picture of the NSTTF site. The NSTTF consists of 220 heliostat mirrors (37.2 m^2 each), 64 of which will be used by STACEE.

The heliostats reflect the Cherenkov light onto secondary mirrors on a central tower. Four 2 m diameter secondary mirrors viewing different parts of the heliostat field will be used. Light reflected from each secondary mirror

Figure 1.2: Secondary mirror and camera.

is imaged onto a photomultiplier tube (PMT) camera. Each heliostat is viewed by a single PMT. Figure 1.2 shows a picture of a secondary mirror and its associated camera.

Each camera consists of 16 PMT can assemblies (or modules) mounted on a slotted plate. Each module holds an assembly which comprises an acrylic light concentrator followed by a PMT. The concentrators are Dielectric Totally Internally Reflecting Concentrators (DTIRCs). An in-depth description of PMTs and DTIRCs is provided in the next chapter. The PMT and concentrator are held together in a hollow metal cylinder which has an edge ring

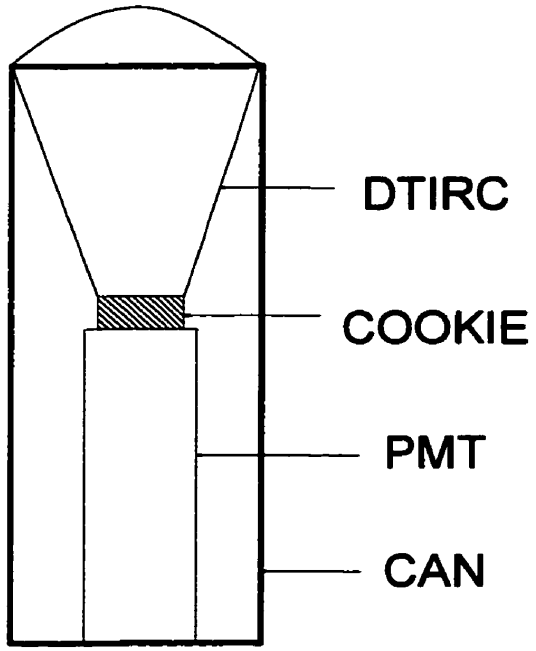

Figure 1.3: Diagram of a module of the STACEE camera. (*Not to scale*).

at one end and a threaded disk at the other. The disk pushes the concentrator and PMT together; they are separated by a silicon rubber cookie which provides good optical and mechanical coupling. Figure 1.3 shows a diagram of a module of the camera.

The camera converts the Cherenkov photons to analog pulses which are processed by other parts of the detector, mainly electronics modules. The precise timing and size of these pulses contain the sought after information about the primary gamma ray photon that initiated the extensive air showers. By using the time of arrival of each photon we can reconstruct the wavefront of the extensive air showers and determine the origin of the source. The

size of the pulses should be related to the energy of the primary gamma ray photon, but the exact relation is not known yet. Theoretically, photons at a given energy, crossing the front face of the camera at a random position, should produce the same pulses, as long as they are within the field of view of the camera; ie, the response of the module should be constant across its surface. In order to verify this prediction, a special instrument was designed and built at McGill University. In this thesis we describe how this instrument functions, and how it can be used to study the response of a module of the camera to different lighting conditions. Different tests were performed with the instrument, and the results are presented and discussed in the last chapters.

Chapter 2

The STACEE camera

As mentioned in the introduction, the camera consists of PMTs and concentrators held together and separated by a silicon rubber cookie. In this chapter we explain what DTIRCs are, and why they are required. We also explain how PMTs function.

2.1 DTIRCs

DTIRCs were introduced in 1987 [5], and were supposed to supplant the compound parabolic concentrators (Winston cones) which had been used in solar energy concentration systems and high-energy Cherenkov light detectors. Although DTIRCs have smaller sizes than Winston cones, they have never been used for such applications. Recently, NASA has evaluated the feasibility of utilizing DTIRCs for solar heat receivers operating at temperatures up to

2500 K in the NASA-MSFC "Shooting Star" flight experiment [6]. STACEE uses DTIRCs to define the field of view of each element of the camera and to increase the collection area of each PMT.

DTIRCs combine front surface refraction with total internal reflection from the sidewall to achieve concentrations close to the theoretical maximum limits. When a light ray is incident on the front surface, it is refracted according to Snell's law, and then reaches the sidewall or goes straight to the far end. If the light ray is within the angular field of view of the DTIRC, it is reflected back into the DTIRC by total internal reflection, and it gets out through the exit aperture. In the case where the light ray is beyond the acceptance angle, it exits through the side profile. Figure 2.1 shows trajectories of light rays at the limit of the acceptance angle.

By choosing the appropriate acceptance angle, we can reject light which does not come from the heliostats, and thereby decrease contamination from night sky background. DTIRCs can be designed to have different acceptance angles; the arc angle of the curved front surface and various subsidiary conditions that we may wish to impose on the outgoing light rays determine the form of the sidewall [5]. Figure 2.2 shows 2 DTIRCs with different arc angles and a Winston cone (DCPC); they all have the same acceptance angle. The front surface curved DTIRCs are much smaller than the Winston cone. Because they are easier to produce, the STACEE group decided to use straight side DTIRCs. Figure 2.3 shows a picture of a DTIRC used by STACEE. Three models of DTIRCs with different acceptance angles were

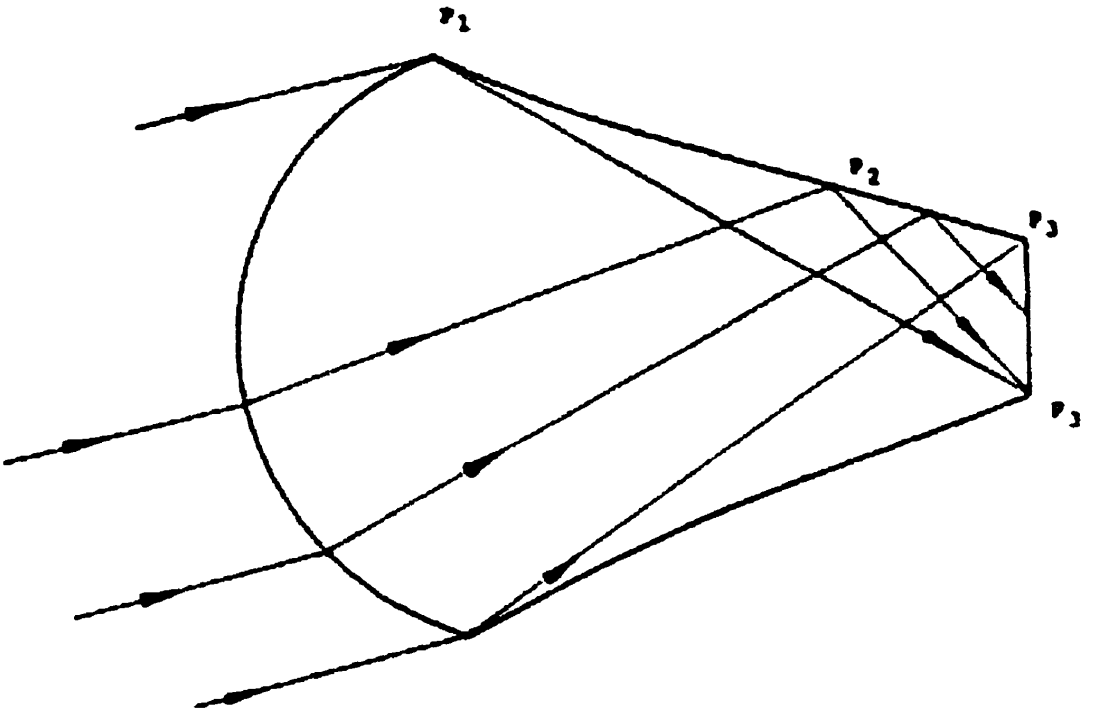

Figure 2.1: Trajectories of light rays at the limit of the acceptance angle.

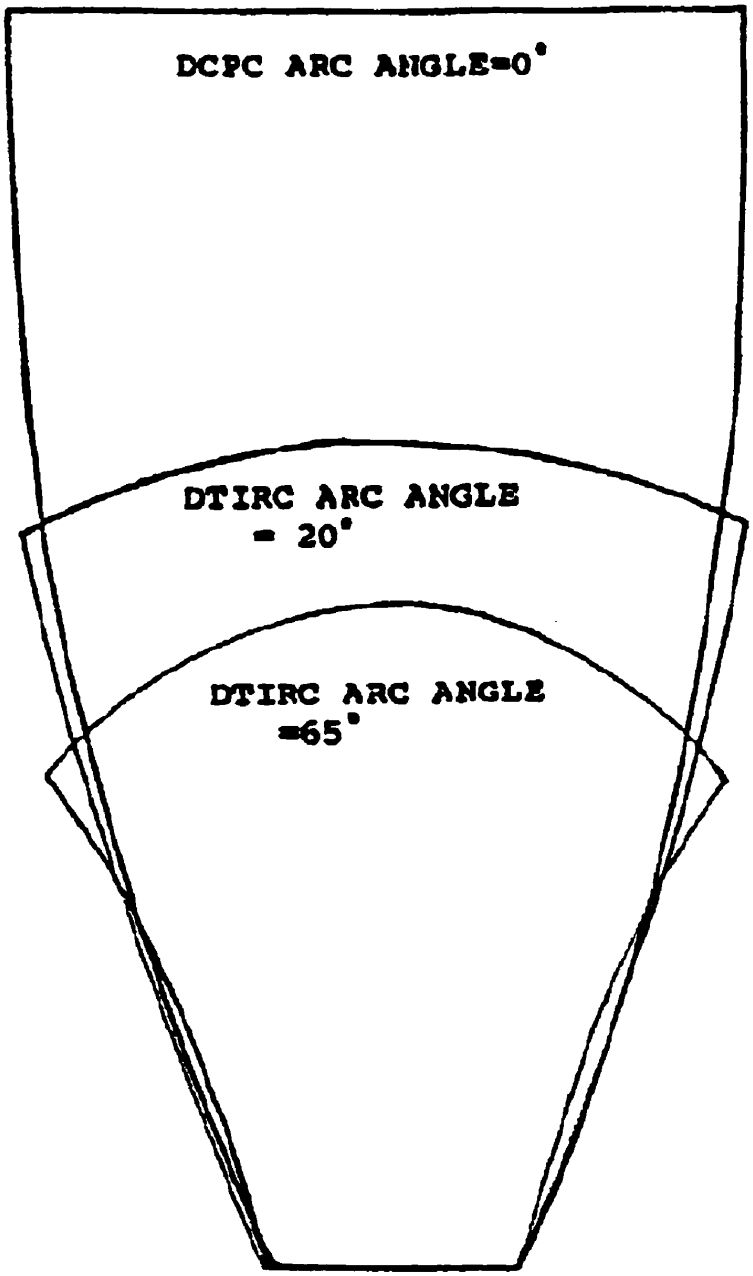

Figure 2.2: Two DTIRCs with a different front surface arc angle and a Winston cone. They all have the same acceptance angle.

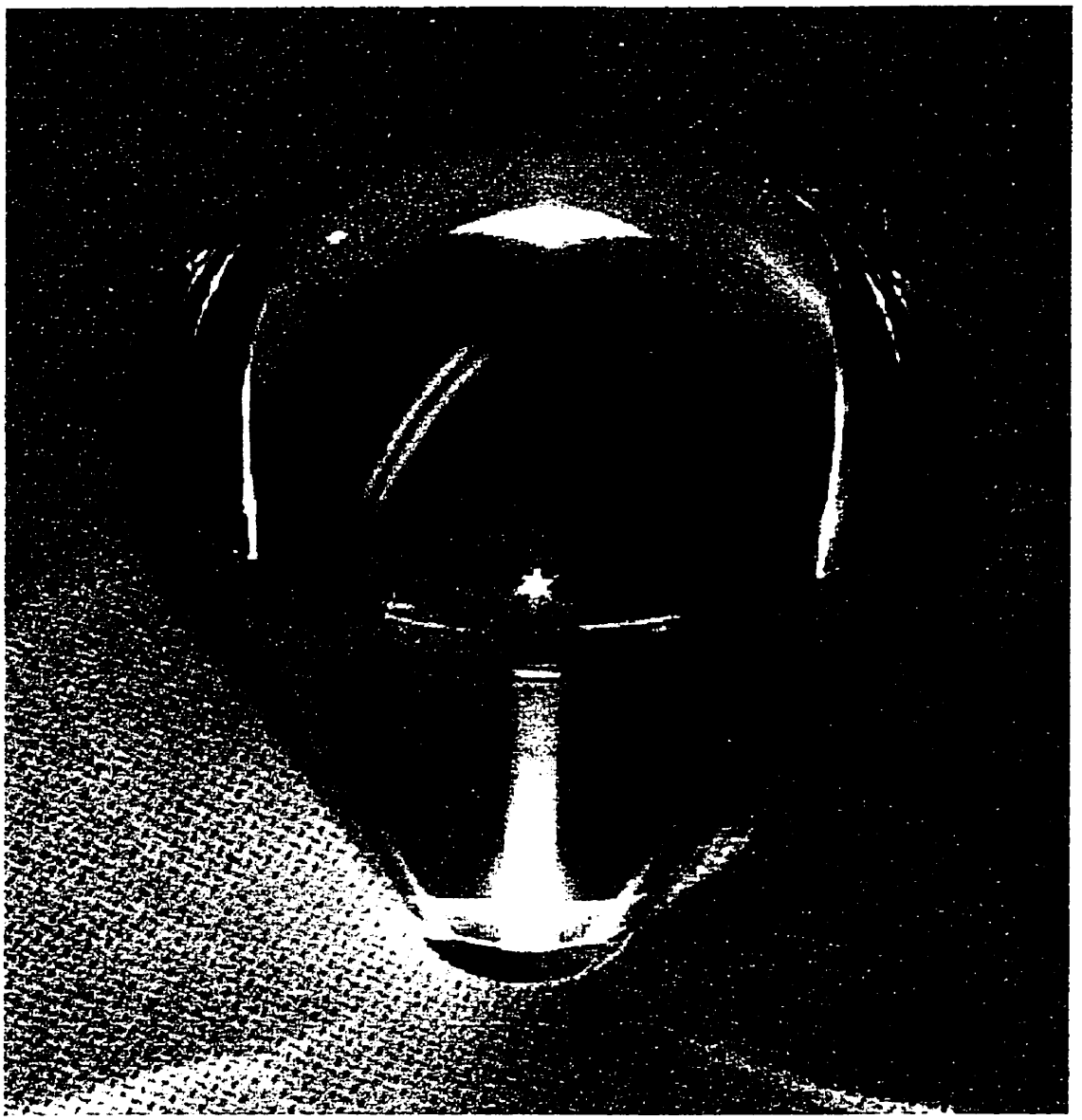

Figure 2.3: Picture of a DTIRC used by STACEE.

built. The smaller DTIRCs had a 19° acceptance angle, the medium were 24°, and the larger were 28°. To a good approximation, the field of view of each heliostat is given by the angle subtended by the secondary mirror on the tower when viewed from that heliostat. Thus, the heliostats' fields of view ranges from 0.5° (for the most distant heliostats) to 0.9° (for the closest heliostats). Because the amount of night sky background light each heliostat sees varies with its field of view, it is desirable to equalize the field of views of all heliostats as much as possible. Therefore, PMTs viewing heliostats closest to the tower are matched with DTIRCs that have a field of view of 19°, whereas PMTs viewing heliostats farthest from the tower are matched with DTIRCs having a field of view of 28°.

2.2 PMT

A photomultiplier tube is a photosensitive vacuum device comprising a photoemissive cathode (photocathode), a photoelectron collection system, and one or more stages of electron multiplication using secondary emission electrodes (dynodes) between cathode and anode [7]. The diagram of a typical PMT is shown in Figure 2.4.

Each time a photon hits the photocathode, there is a probability that an electron is emitted via the photoelectric effect. The ratio of the number of emitted electrons to the number of incident photons is called the *quantum efficiency*. Factors affecting it are the wavelength of the incident light and the

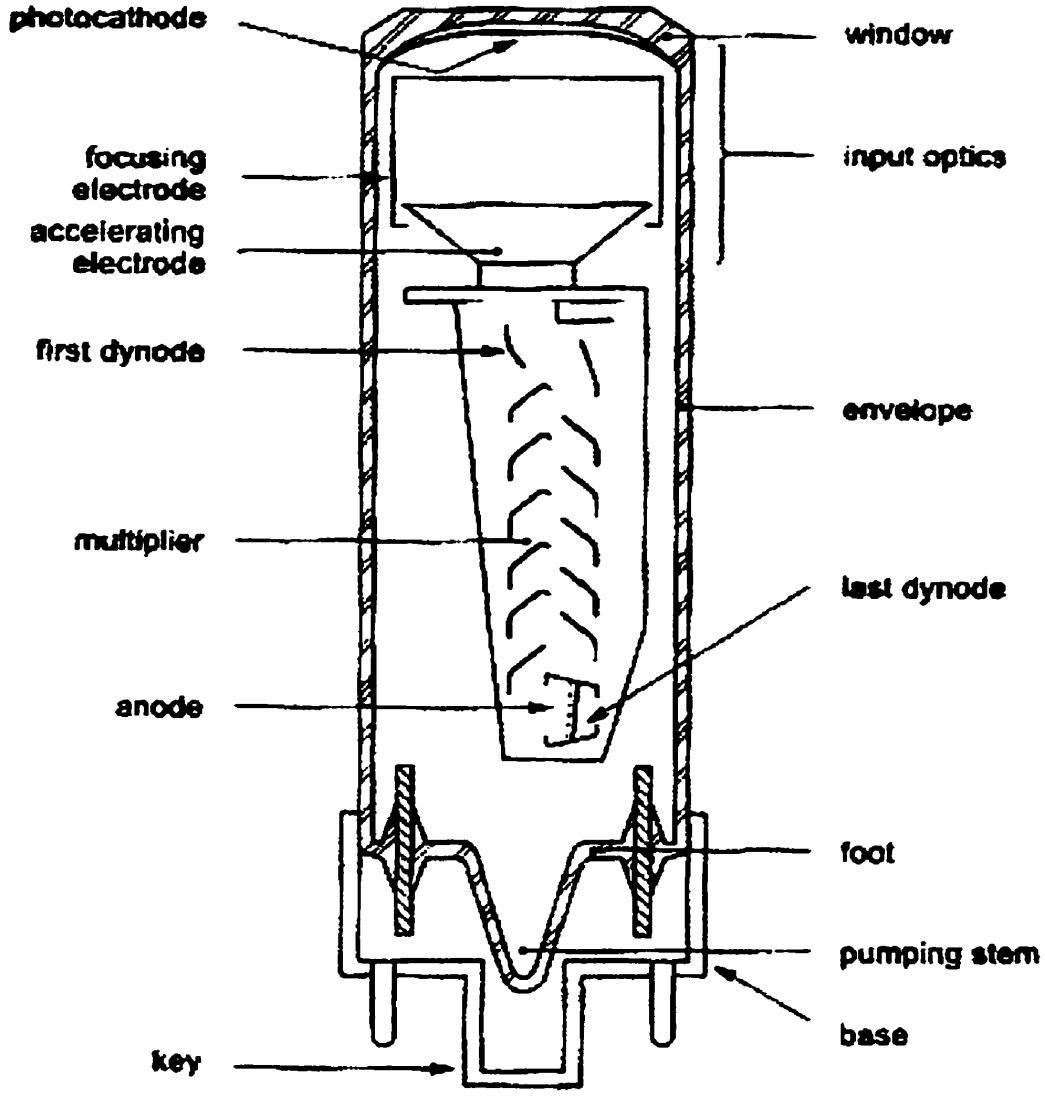

Figure 2.4: Diagram of a typical PMT.

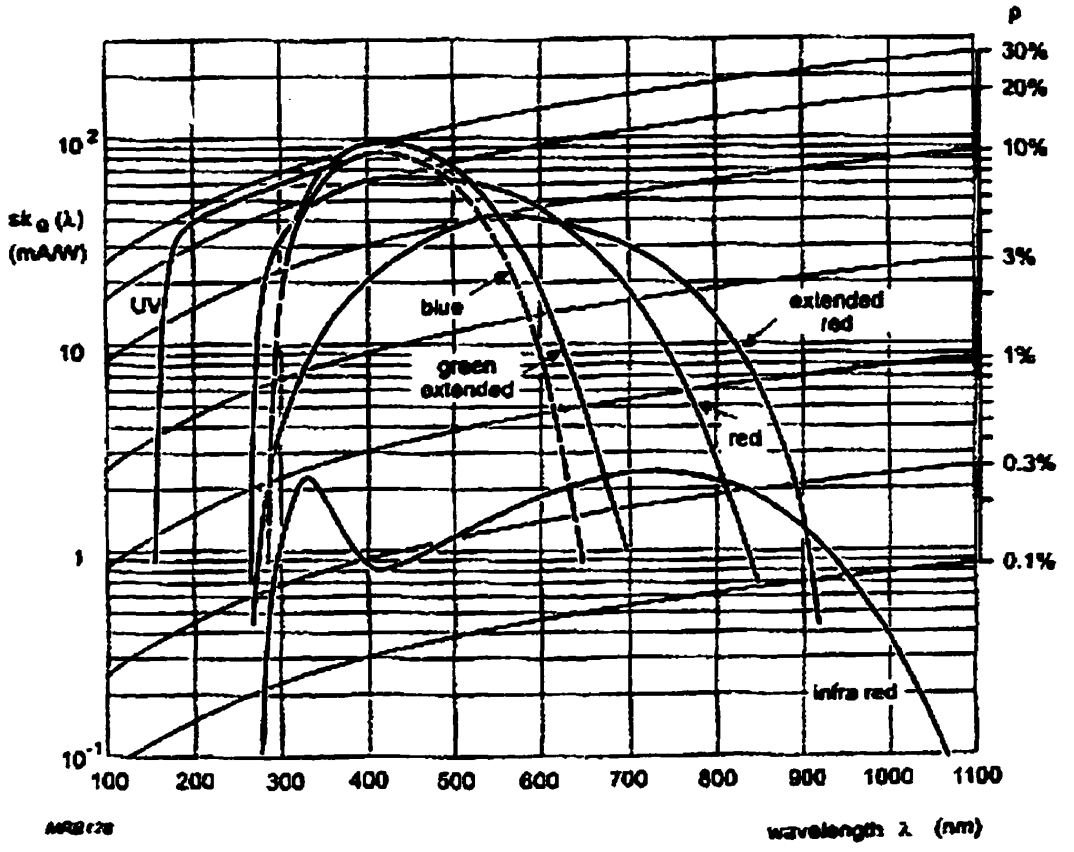

Figure 2.5: Spectral sensitivity characteristics for various photocathode types. Curves of uniform quantum efficiency, ρ, are shown for reference.

composition and thickness of the photoemissive material. Figure 2.5 shows the spectral sensitivity characteristics for various photocathode types. Also shown are curves of uniform quantum efficiency.

The emitted electron is directed and accelerated toward the first dynode, where it transfers some of its energy to the electrons in the dynode. This causes more electrons to be emitted (*secondary emission*) and further accelerated, creating an electron cascade. At the anode, this cascade is collected

to give a current which can be analysed. The gain of a PMT is the ratio I_a/I_k, where I_a is the anode current due to a cathode photocurrent I_k:

$$G = \frac{I_a}{I_k}.$$

The gain varies with temperature, incident-light wavelength, and mean anode current [8].

The STACEE experiment uses Philips XP2282B PMTs with voltage divider VD182K/C. These tubes have a bialkali semi-transparent photocathode on a glass window. Their spectral range is 300–650 nm, with a peak sensitivity at 400 nm. At this wavelength, the stated quantum efficiency is 28%. A supply voltage of 1700 Volts spread over 8 dynodes stages was used for all measurements done at McGill. At this voltage the gain is typically 1.5×10^5.

Chapter 3

The instrument

The Cherenkov photons produced by the extensive air showers are converted to analog signals by the STACEE cameras. To extract the information contained in these signals, measurements of the response of individual modules to different lighting conditions in a controlled environment is required. To carry out these measurements, a special instrument was designed and built at McGill. In the next sections we present the different components of this instrument, and we explain how to control the position of the light source.

3.1 Description of the instrument

The main purpose of this instrument is to study the response of a module of the STACEE camera (or a single PMT without a DTIRC) under different lighting conditions. By using a narrow beam of monochromatic light,

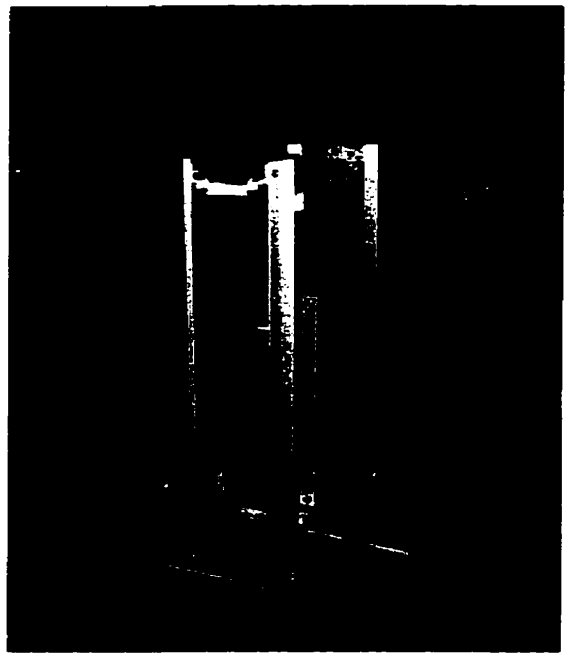

Figure 3.1: Picture of the instrument. The upper platform supports the light source, and the lower platform supports the module or a single PMT. The grey object shown in the picture is a piece of foam designed to hold the PMT in place.

we can obtain a picture of the module's response to light at different angles and wavelengths. The instrument consists of two platforms that can translate at right angles to each other in order to raster scan the module being studied. The lower platform translates in the X direction, and supports the module. The other platform translates in the Y direction and supports the light source. The light source can be rotated to illuminate the detector at different angles. These platforms are enclosed in a light-tight box shown in Figure 3.1. A diagram of the instrument is also shown in Figure 3.2.

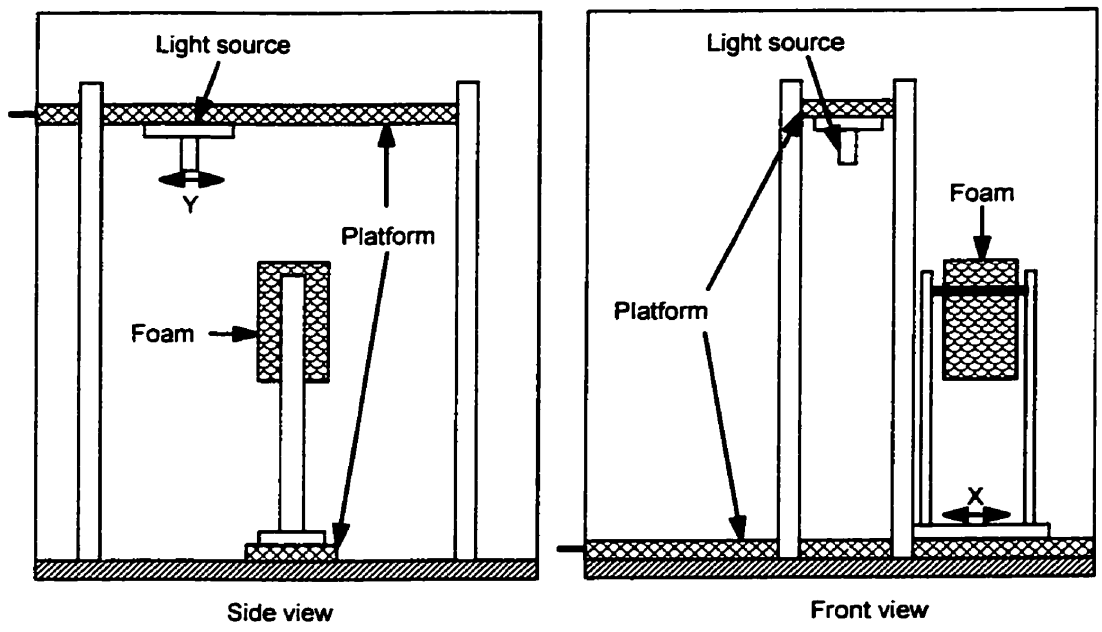

Figure 3.2: Diagram of the instrument.

3.2 Control of the instrument

The most accurate way to position the detector and light source was to use stepping motors coupled to the translation platforms. A PC running DOS was used to optimize the speed of data acquisition, and to send commands to the stepping motors. The following two sections contain information on the stepping motors and on the electronics used for the data acquisition.

3.2.1 Stepping motor characteristics

Stepping motors[1] and translator modules[2] were used to control the position of the light source. The translator modules electronically converted TTL input pulses into drive signals of the proper switching sequence and currents to drive the stepping motors. The resolution was 1.8°, with 200 discrete positions in a full 360° rotation. The stepping motors were mechanically coupled to the platforms responsible for translating the detector and light source. A full rotation of the shaft produced a translation of 2 mm in the X direction and 1.6 mm in the Y direction; thus the resolution was 4 μm in X, and 3.2 μm in Y. Figure 3.3 shows a picture of a translator module and stepping motor used to control the position of the light source.

3.2.2 Electronics and computer interface

Figure 3.4 shows a diagram of the electronics system used for controling the position of the stepping motors and for data acquisition. A PC running DOS was connected to a CAMAC Crate Controller[3] via an interface card[4]. An Output Register[5] generating standard NIM level pulses was used to send information to the stepping motor controllers and to trigger a pulse generator[6]. The amplitude of the output of the pulse generator could be adjusted be-

[1]SLO-SYN® MO61 steping motor
[2]SLO-SYN ® 230-PT translator module
[3]DSP Technology CAMAC Crate Controller, model 6001
[4]DSP Technology IBM PC interface card, model PC004
[5]McGill HEP output register
[6]Berkely Nucleonics Corp. pulse generator, model number 8010

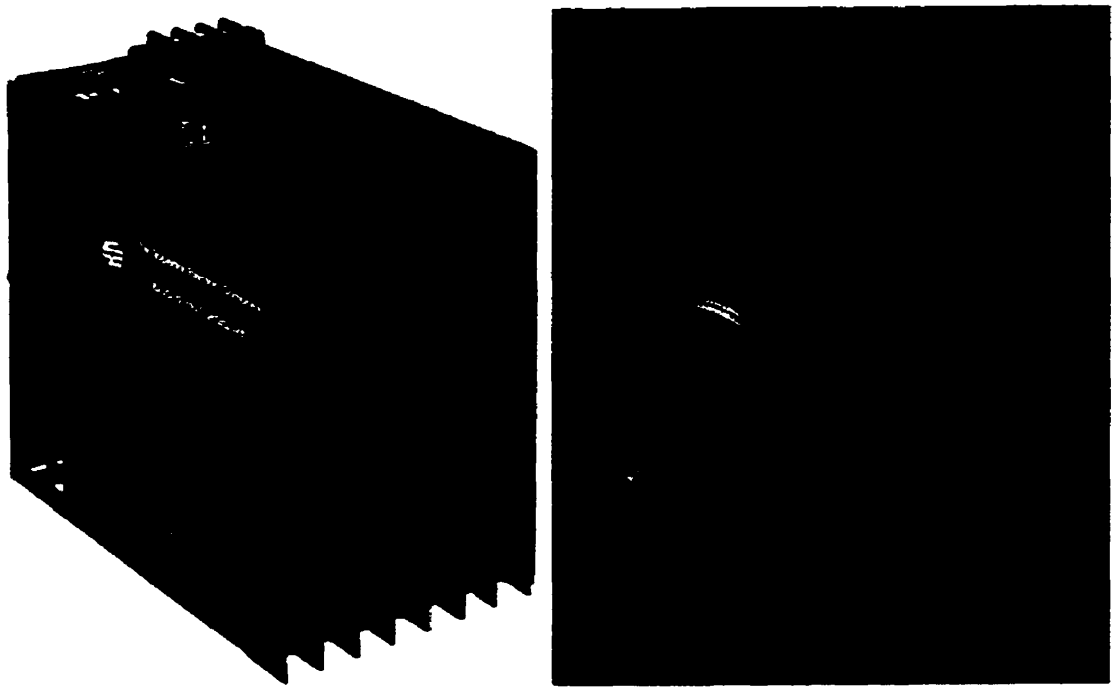

Figure 3.3: Picture of a translator module and stepping motor used to control the position of the light source.

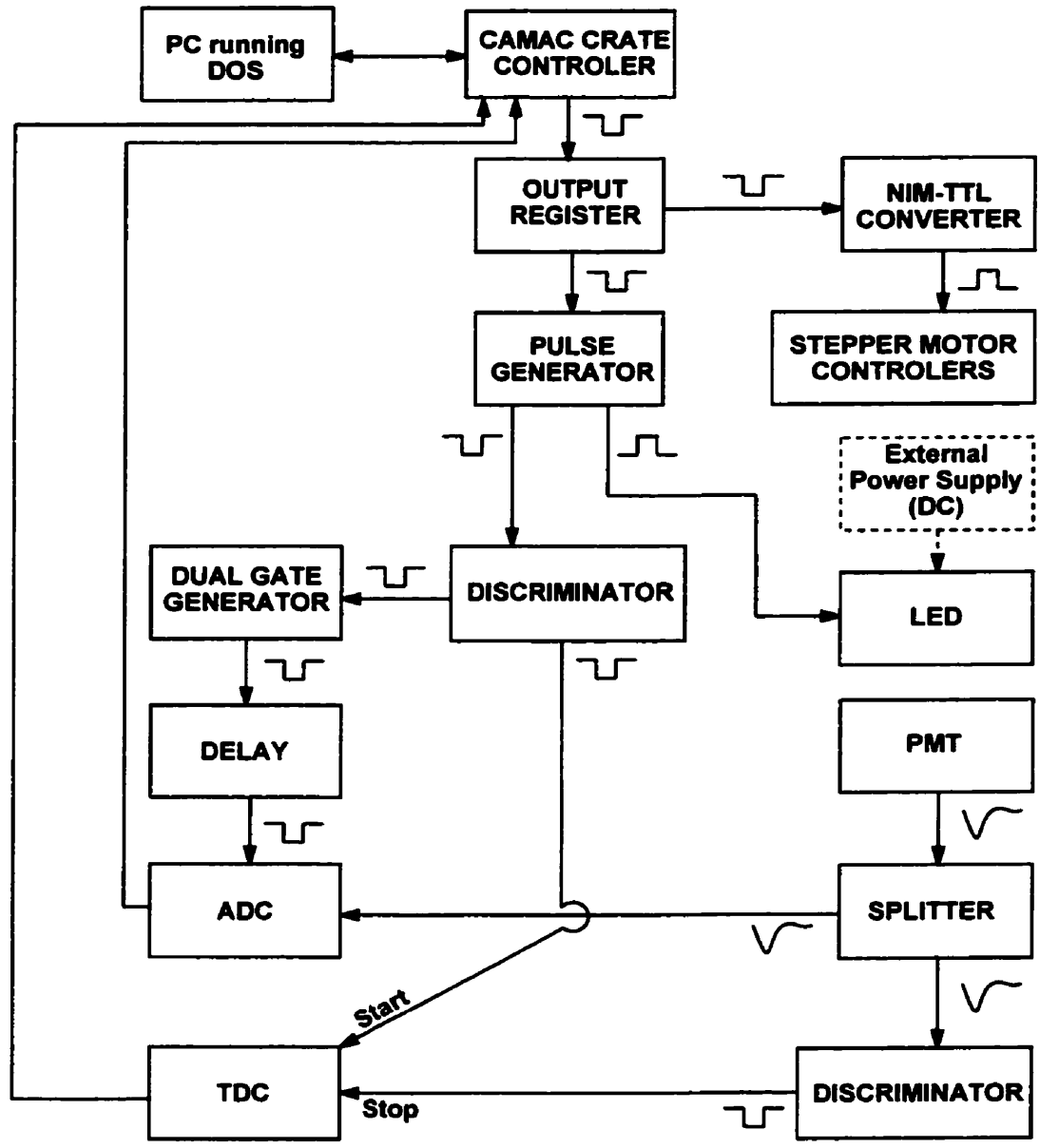

Figure 3.4: Instrumentation used for data acquisition.

tween 0 and +5 Volts, and the duration of the pulse could be made as small as 10 ns. This positive voltage pulse was used to power the Light Emitting Diode. For a DC mode of operation, an external power supply was used instead of the pulse generator.

The negative output of the same pulse generator was a standard NIM level. It was used to start a TDC[7] and to generate an ADC gate using a programmable gate generator[8]. Figure 3.5 shows an oscilloscope trace of a typical PMT pulse with an ADC gate. Once appropriately delayed, the gate was sent to an ADC module[9]. The response of the PMT was split into two equal analog signals; the first was discriminated[10] and used to stop the TDC, the second was sent to an ADC channel. The ADC and the TDC values were then read and stored in a computer file.

3.3 Different light sources

When collimation of the light beam is important, compact lasers are the best light sources available. The diameter of the beam can be easily adjusted with a diaphragm, and the divergence of the beam is generally negligible. Lasers are also available in different colors, but they are expensive devices. An alternative to lasers is a collimated LED. LEDs are cheap and available in different colors. However, they are divergent light sources, and they need

[7]Lecroy 2228A TDC module
[8]Lecroy 2323A Programmable Dual Gate Generator
[9]Lecroy 2249W ADC module
[10]Lecroy 623B Octal Discriminator

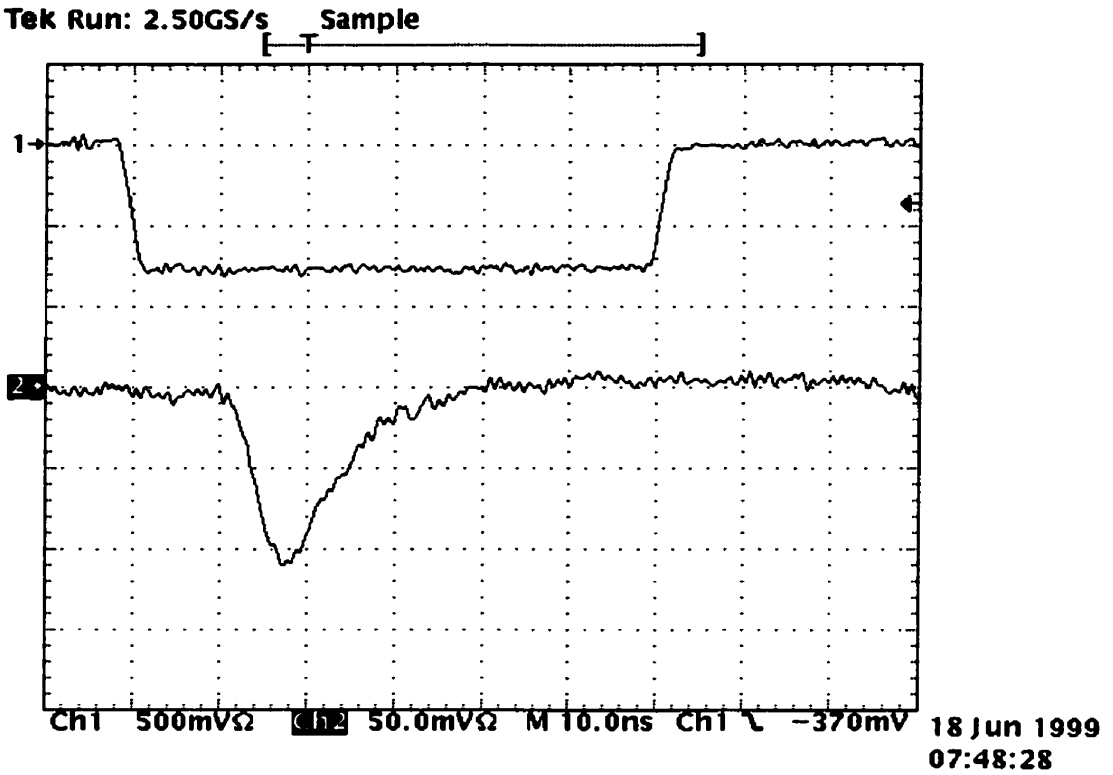

Figure 3.5: Oscilloscope trace of a typical PMT pulse obtained with a blue pulsed LED. The first trace is the ADC gate, and the second trace is the PMT pulse of approximately 100 mV of amplitude.

to be coupled to a collimator. The collimator reduces the divergence of the beam, but it also decreases its intensity. This is not a problem when the LEDs are used in a continuous (DC) mode, but it is a concern when the LEDs are pulsed. Figure 3.5 shows the response of the PMT when the light source is a blue pulsed LED. The first trace represents the ADC gate, and the second trace is the actual PMT pulse.

When collimation of the light source is not required, other alternatives are available. Larger lasers can be coupled to an optical fibre which terminates

inside the box. We used a pulsed nitrogen dye laser and we did tests at different wavelengths. LEDs can also be used, and they are more interesting than lasers because we can easily control the intensity of the light pulse. Overall, we found that LEDs are the most useful sources for this instrument.

Chapter 4

Results

As described in the previous section, a module of the STACEE camera is mainly composed of 2 elements: a DTIRC and a PMT. The module can be thought of as a black box with an input and an output. We would like to find the transfer function linking the input to the output without worrying about what is happening inside the box. One could place a module inside our instrument and measure its response to different lighting conditions. That procedure would be perfectly fine, and it is all that is required for modeling the experiment. However, a reductionist approach to understanding how the module is working could reveal unexpected results. It was more appealing to us to chose the reductionist approach, and unexpected results were indeed observed.

4.1 Analysis of PMTs

We first took the module apart and studied the response of the PMT itself to different lighting conditions. Results from these experiments are presented in this section.

4.1.1 Stability of PMT over time

A two-dimensional scan of the surface of a module at a fixed angle takes approximately 20 minutes. During the scan, we measure the response of the module to a narrow beam of monochromatic light, whose intensity remains constant for the duration of the scan. To get a "*map*" of the sensitivity of the module it is essential that the gain of the PMT remain the same during the scan. An increase (or decrease) of the gain would imitate a better (or worse) sensitivity. A drift of the gain during the scan would therefore spoil our results. As mentioned in section 2.2, the gain varies with temperature, incident-light wavelength, and mean anode current.

Since we are using a source of light which does not change appreciably during the period of the scan, the contribution of this factor to the change in gain is negligible. According to the manufacturer of the PMTs used by STACEE when the flux to which a PMT is exposed gives rise to a mean anode current of less than 10 μA the gain is usually stabilized after about 10 or 15 minutes [8]. When a high voltage is first applied to the voltage divider heat is generated and the temperature of the PMT increases.

To investigate the combined effects of temperature changes and mean anode current on the gain of the PMT, we illuminated the photocathode with a constant light source (red laser[1]) for an extended period of time. A thermocouple[2] was used to measure the temperature of the PMT as a function of time. Since the heat was generated at the base of the PMT, a gradient of temperature was observed (hotter at the base, colder at the photocathode). We decided to record the temperature at the base of the PMT where the change in temperature was the larger. The PMT was initially at room temperature, and its temperature gradually increased until it reached its operational point (6 degrees Celsius above room temperature) after 40 minutes. After 1 hour, the voltage on the PMT was turned off, and the instrument was opened for $\sim$ 1 minute. The same measurement was repeated for another half-hour. Figure 4.1 shows the result of this experiment. The upper panels show the first data set. The mean number of ADC counts gradually decreased during the first 40 minutes ("warm-up"), and remained constant for the rest of the run. After cycling the voltage on the PMT and opening the instrument, the mean number of ADC counts remained constant (panel D). The fact that the data in panel D is consistent with being a flat distribution ($slope = -0.003 \pm 0.01$) implies that the gain of the PMT was likely to remain constant for the duration of the run, providing that the PMT had enough time to warm up.

[1]Small pencil laser available at Radio Shack
[2]Fluke Thermocouple Module, model 80TK

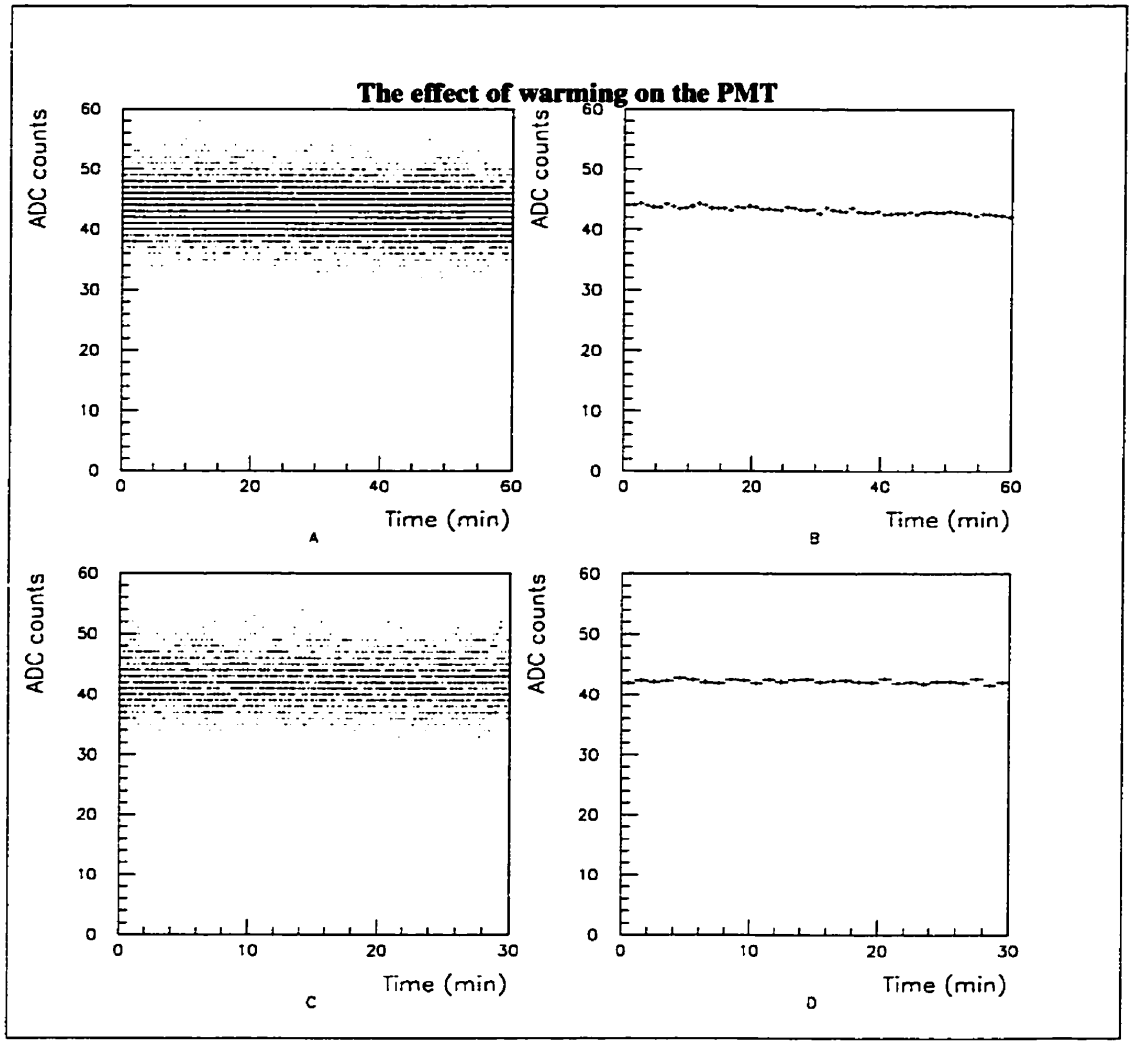

Figure 4.1: Stability of PMT as a function of time. Panels A and C show the raw data for two consecutives runs, whereas panels B and D show the time average of these runs for 1 minute periods.

4.1.2 Two-dimensional scan with red laser

A two-dimensional scan of the photocathode was performed using a red laser at 0° inclination (vertical). The diameter of the continuous (DC) light beam was <1 mm, and its divergence was negligible. A special ADC module[3] was used to measure the DC anode current coming out from the PMT. The laser was positioned at $\sim$ 1 cm from the photocathode, and data were taken at each point on a grid with unit element of 0.5 mm $\times$ 0.5 mm. At each point 1000 measurements were taken, which gave us a

$$\frac{\delta_Q}{\langle Q \rangle} \leq 1\%$$

where δ_Q is the error on the mean, and Q is the pedestal-subtracted ADC value. The pedestal was the sum of the electronics pedestal, which was constant, and the dark current produced by the PMT. The width of this distribution was typically 1 ADC count.

Figures 4.2 and 4.3 show the result of a two-dimensional scan performed on 2 PMTs of the same model. The Z axis showing the tube's response in ADC counts can be thought of as a convolution of the quantum efficiency, the photoelectron collection efficiency and the single photoelectron gain. It can be seen to be very non-uniform across the face of the tube. Although the responses are similar there are noticeable differences. We were expecting

[3]Lecroy 2249A ADC module. This type of ADC module measures the amplitude of signals which are DC coupled. Another type of ADC module (2249W) measures the amplitude of signals which are AC coupled.

to find a uniform distribution, so this result was surprising. Repeating the experiment showed that the results were reproducible.

4.1.3 Multiwavelength analysis with LEDs

The response of the photocathode to red light prompted us to further investigate other wavelengths (these PMTs are optimized for blue light). LEDs, which are inexpensive and available in different colors, were the best candidates for this task. We built a small collimator and we installed the LED in the instrument. The diameter of the light beam was measured to be $\sim 2\ mm$ on the surface of the photocathode and it was a continuous beam (DC).

Figure 4.4 shows the result of a multiwavelength analysis of the photocathode. Because of the larger diameter of the light beam, details of the structure shown in Figure 4.2 were smoothed out. However, the resemblance between the scan with the red laser (Figure 4.2) and the one with the 700 nm LED strongly suggests that these results are consistent with each other. As suspected, the behaviour of the PMT is a strong function of the wavelength of the incident photon.

4.1.4 Pulsed LED

The results presented in the previous sections were obtained with the LED in DC mode. In the next test we repeated the two-dimensional scans with a pulsed LED. We believed that pulsed LED would better simulate the

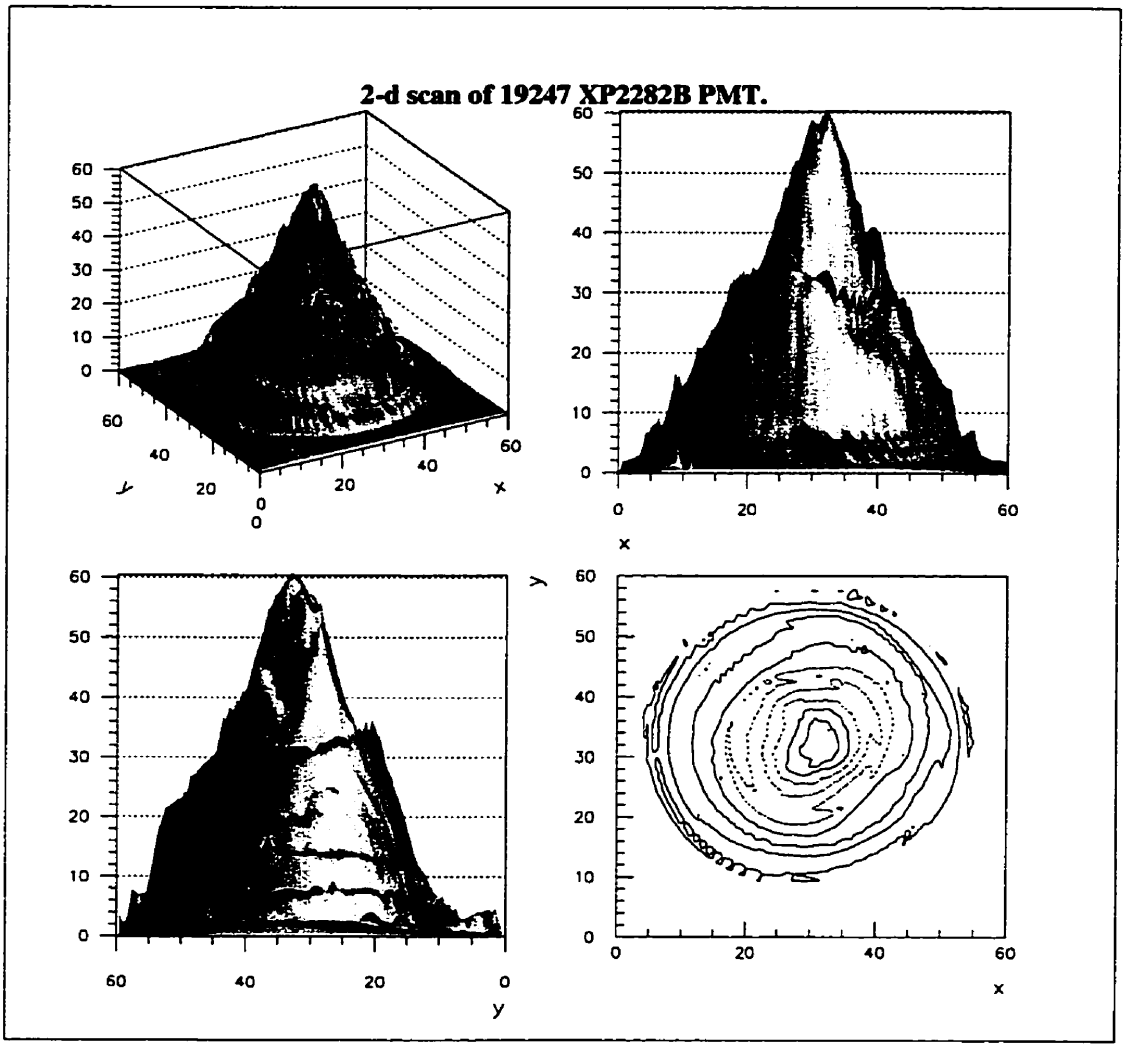

Figure 4.2: Two-dimensional scan of PMT #19247. X and Y axes are in mm, and the Z axis is the number of ADC counts. The lower right panel is a contour plot.

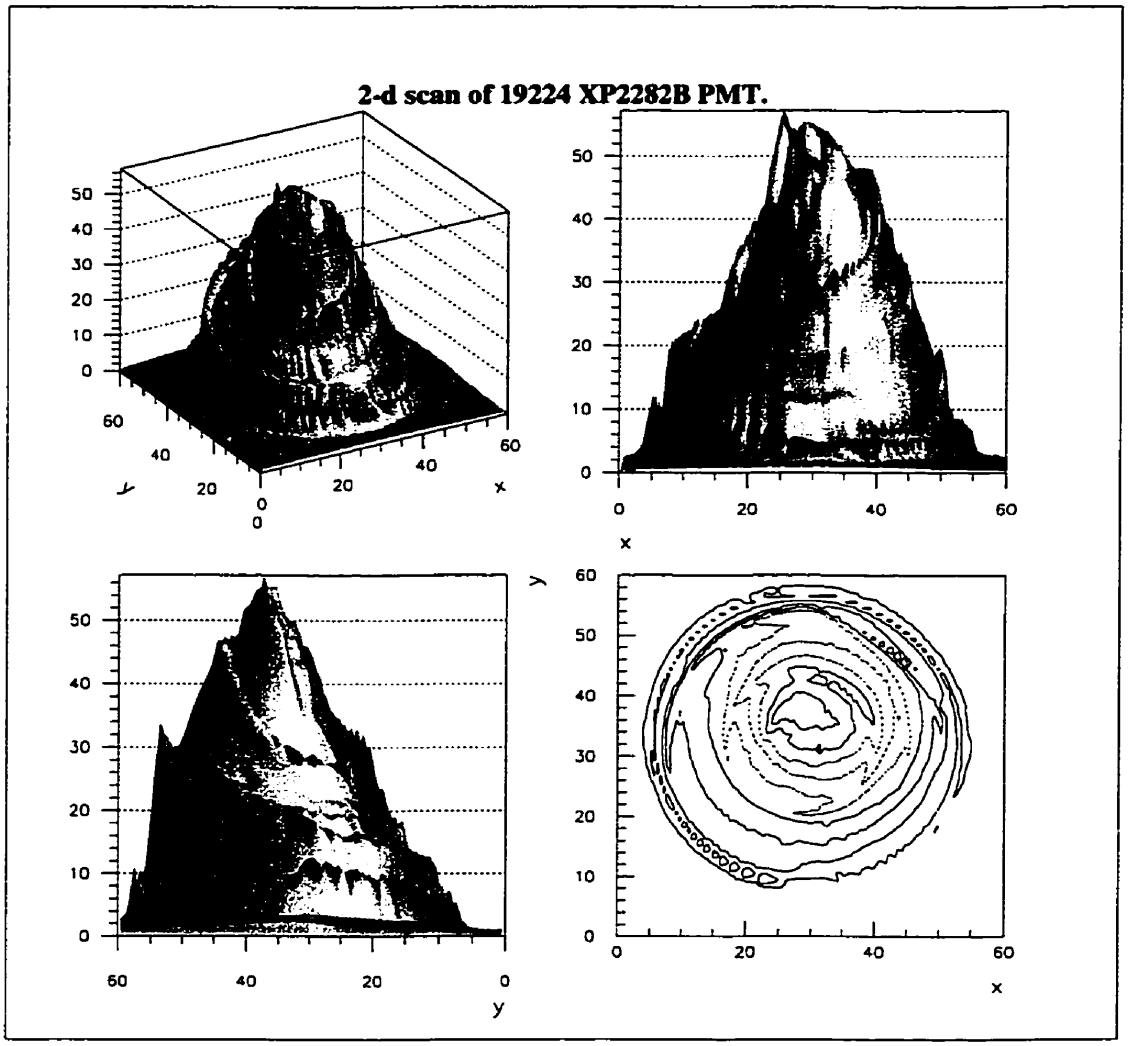

Figure 4.3: Two-dimensional scan of PMT #19224. X and Y axis are in mm, and the Z axes is the number of ADC counts. The lower right panel is a contour plot.

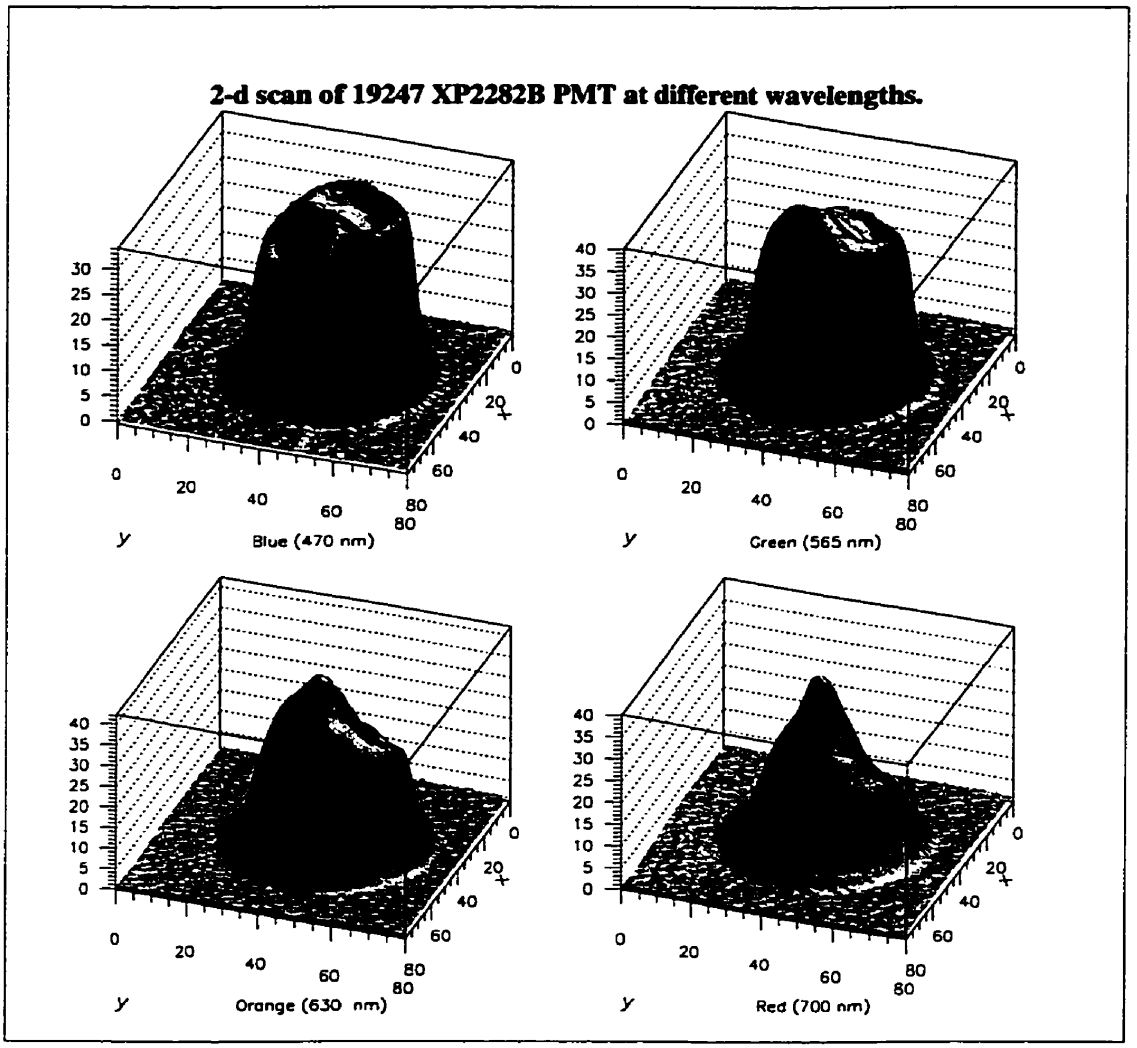

Figure 4.4: Two-dimensional scan of PMT #19247 at different wavelengths. X and Y axis are in mm, and the Z axis is the number of ADC counts.

Cherenkov photons detected by the STACEE detector. The voltage pulses were 10 ns long and the amplitude was 5 volts. Data were collected every 2 mm on a square grid, and at each point 100 measurements were taken so that

$$\frac{\delta_Q}{\langle Q \rangle} \leq 1\%$$

where δ_Q is error on the mean, and Q is the pedestal-subtracted ADC value. These scans were performed for a large number of PMTs and the results are shown in Figures 4.5 and 4.6.

The response of the 12 tubes in Figure 4.5 shows greater variability than the response of the tubes in Figure 4.6. We believe that the response of some of the tubes shown in Figure 4.5 is different because they are older. It is known that the response of the photocathode changes as the tube ages. A feature common to many tubes from both figures is the presence of a bump near the center of the photocathode. We suspect that this structure is somehow due to the method used to deposit the photocathode in the PMT and to the internal structure of the PMT.

4.2 PMT and DTIRC analysis

In the last section we showed that the response of the photocathode was wavelength and position dependent. Although this property of the photocathode is scientifically interesting it does not tell us the response of a complete module of the camera. In this section we show the effect of changing the PMT

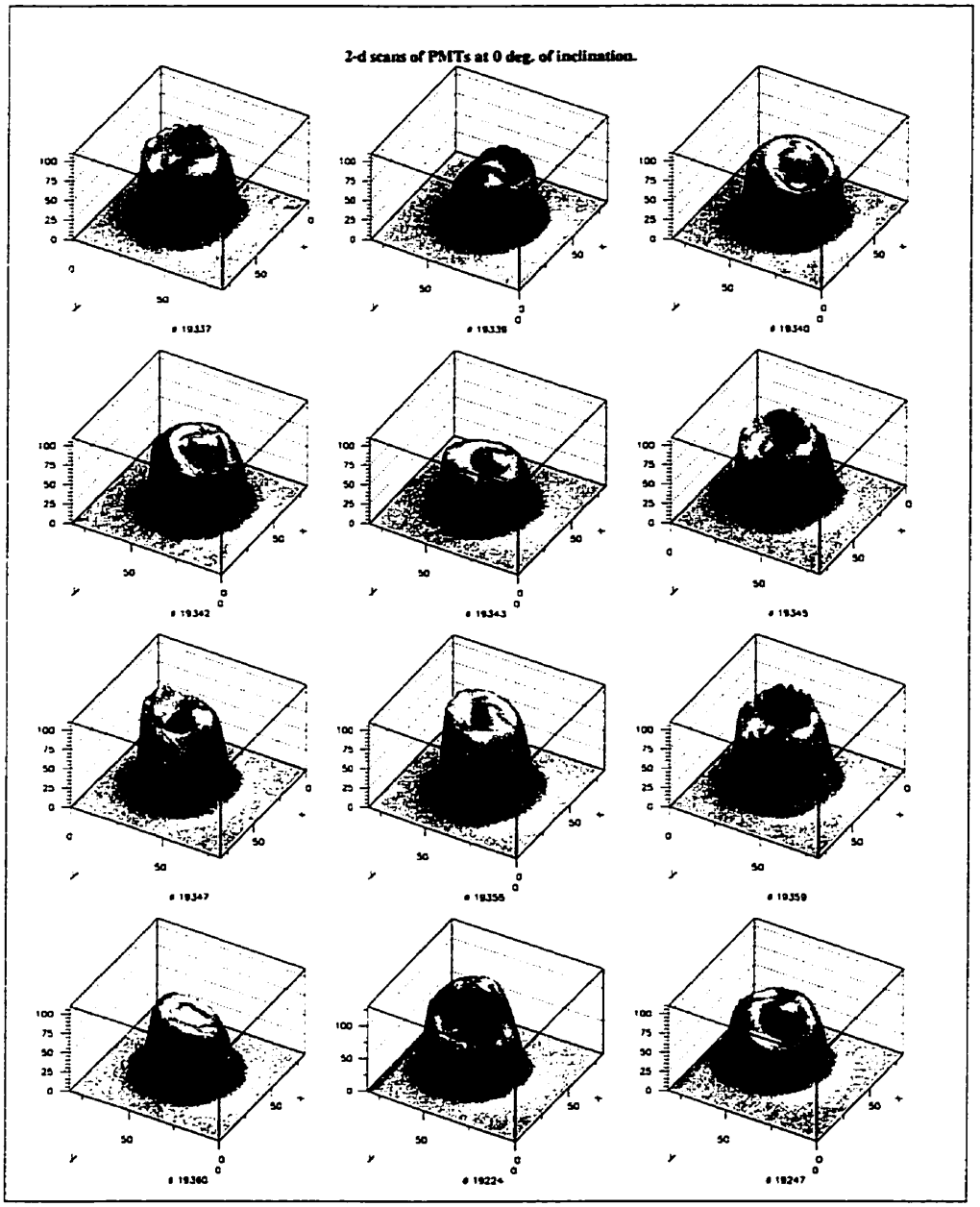

Figure 4.5: Two-dimensional scan of PMTs with a pulsed blue LED. X and Y axis are in mm, and Z axis is the number of ADC counts. Note that the azimuthal orientation of the PMTs is random.

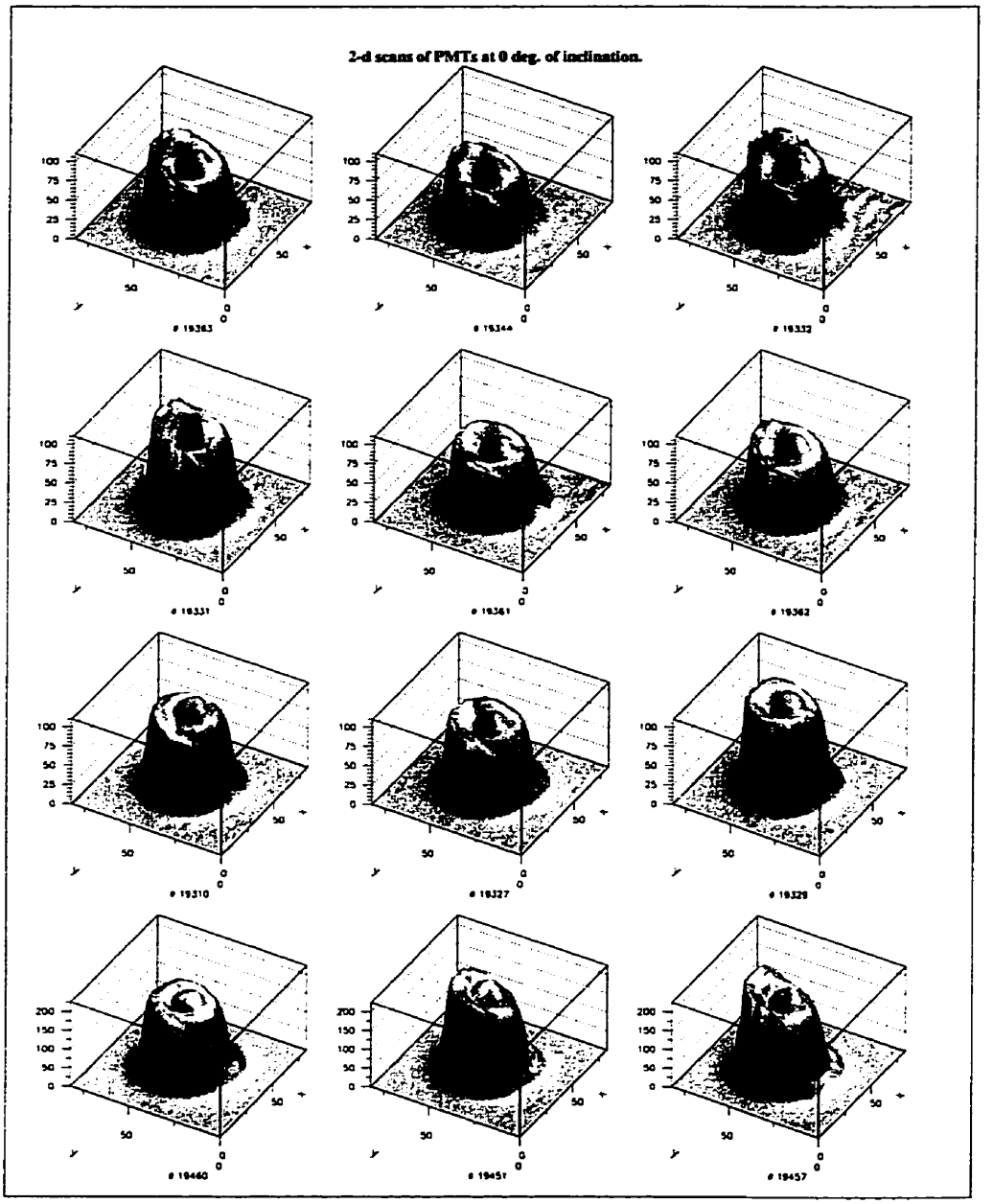

Figure 4.6: Two-dimensional scan of PMTs with a pulsed blue LED. X and Y axis are in mm and the Z axis is the number of ADC counts. All the PMTs have the same azimuthal orientation, which means that the structure is probably related to the physics/structure of the PMT, not of the apparatus.

or the DTIRC on the response of a module of the camera.

4.2.1 Changing the PMT, same DTIRC

By measuring the response of 24 PMTs we found that there was tube to tube variability. In order to investigate how this variability would affect the overall response of a module of the camera, we examined the same DTIRC with different PMTs. We selected a DTIRC with the smallest acceptance angle (19°) and scanned a module with a source of blue light at incident angles varying from 0° to 20° in steps of 2°. Figure 4.7 shows the result of scanning PMT #19247. For incidence angles between 0° and 8° the response of the detector was almost flat. As the angle of incidence was increased the response of the camera became less and less uniform. By adding the number of ADC counts over the whole surface of the camera we could get the total response of the camera for a specific angle of incidence. This is shown in the last panel of Figure 4.7 as a function of the angle of incidence. Theoretically the total response should follow a step function; equal to 1 up to the cutoff angle and 0 for larger angles of incidence. Experimentally we see a deviation from the expected step function.

The same experiment was repeated with PMT #19224 and the result is shown in Figure 4.8. The scan at 0° revealed that the response was not as uniform as the response with PMT #19247. Since the same DTIRC was used this could only be attributed to the different response of each PMT. This difference persisted for larger angles of incidence and the overall response was

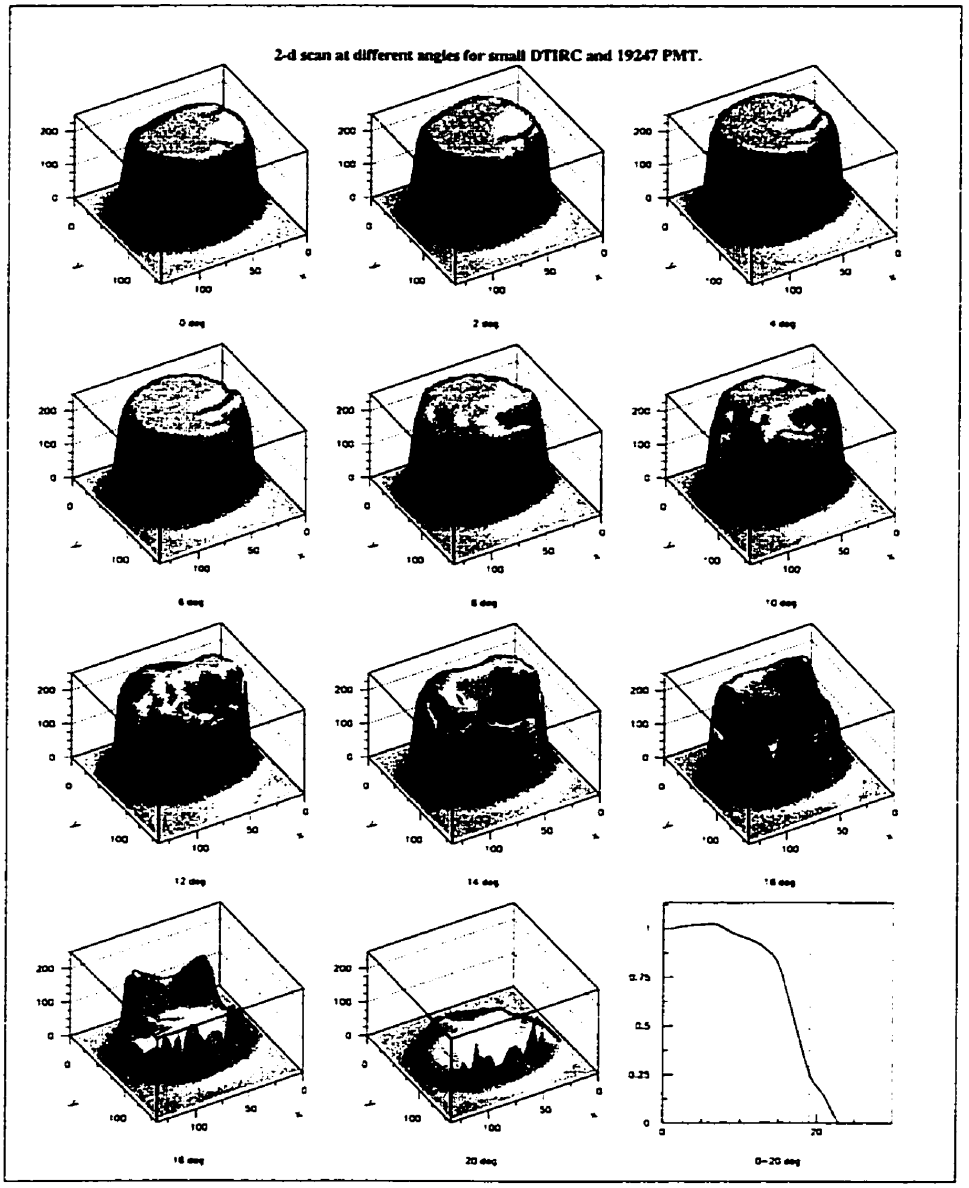

Figure 4.7: Two-dimensional scan of PMT #19247 and a small DTIRC with a pulsed blue LED. X and Y axis are in mm and the Z axis is the number of ADC counts. The last panel shows the total response of the detector as a function of the angle of incidence (normalized to response at 0°). The dotted line shows the nominal cut-off angle.

also slightly different.

4.2.2 Changing DTIRC, same PMT

For the next experiment we kept PMT #19224 but changed the small DTIRC for a medium DTIRC (nominal cut-off 24°). Figure 4.9 shows the results of this experiment. As the incidence angle was increased the response of the module changed in a way similar to what was observed with the small DTIRC. As expected, the cutoff angle of the medium DTIRC was larger than the cutoff angle of the small DTIRC. The wiggle observed around 10° in the total response of the module is not understood at the present time. Notice that the data points are connected with a smooth line (spline fit) which increases the impression of bumpiness. This wiggle was also observed with the small DTIRC, but only with PMT #19224. The PMT may be responsible for this effect.

Figure 4.10 summarizes the results obtained in this section and in the previous one. The total response of a module of the camera is plotted as a function of the angle of incidence for 3 combinations of PMT + DTIRC. As mentioned in section 2.1, the acceptance angle for a module with a small DTIRC should be 19° and 24° for a module with a medium DTIRC. With a small DTIRC the 50% acceptance point of PMT #19247 was $\sim$ 17° and $\sim$ 19° for PMT #19224. When the small DTIRC was changed for a medium DTIRC the acceptance angle of PMT #19224 became $\sim$ 23°. We conclude that there is a spread of the response of PMT + DTIRC from the nominal

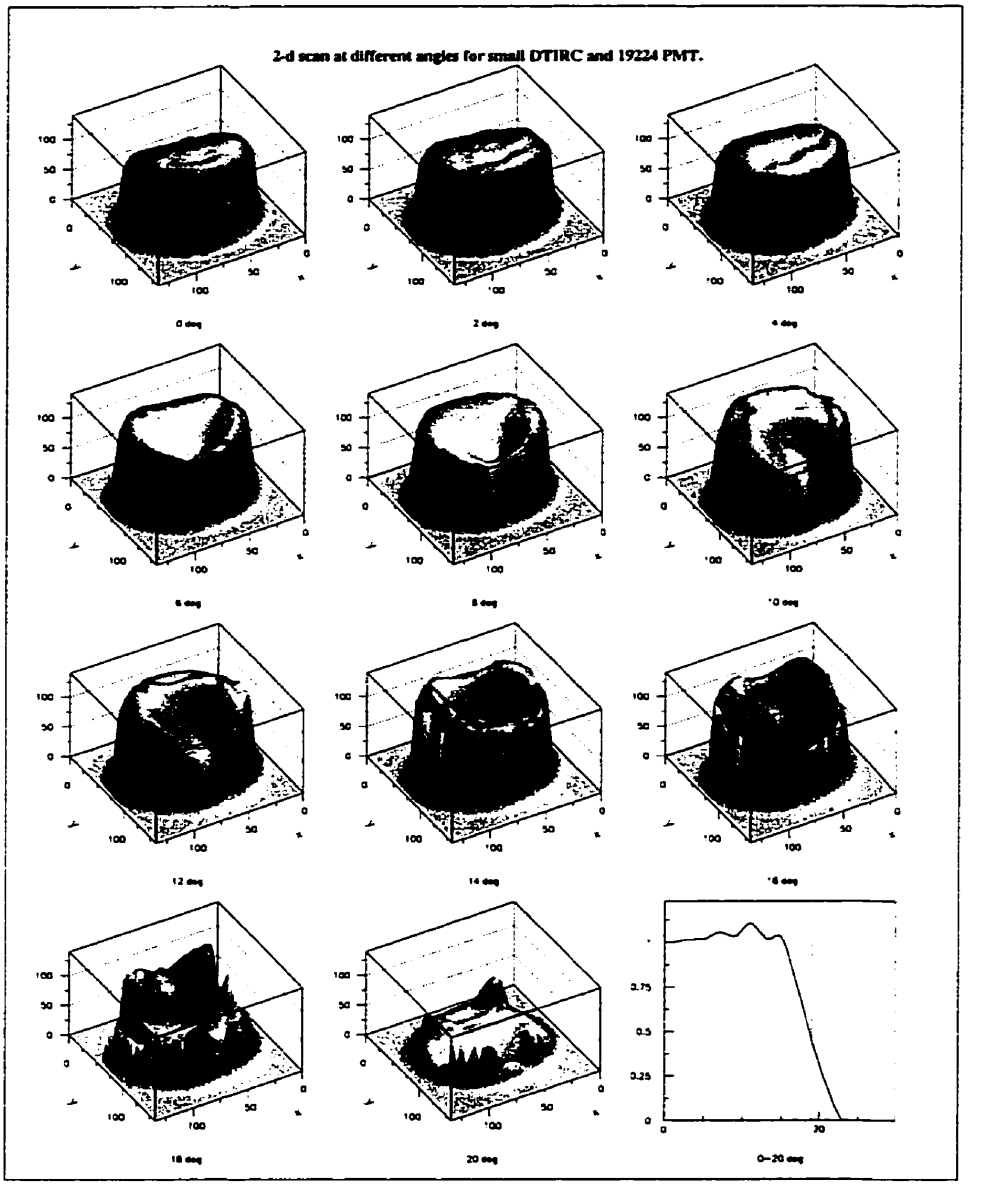

Figure 4.8: Two-dimensional scan of PMT #19224 and a small DTIRC with a pulsed blue LED. X and Y axis are in mm and the Z axis is the number of ADC counts. The last panel shows the total response of the detector as a function of the angle of incidence (normalized to response at 0°). The dotted line shows the nominal cut-off angle.

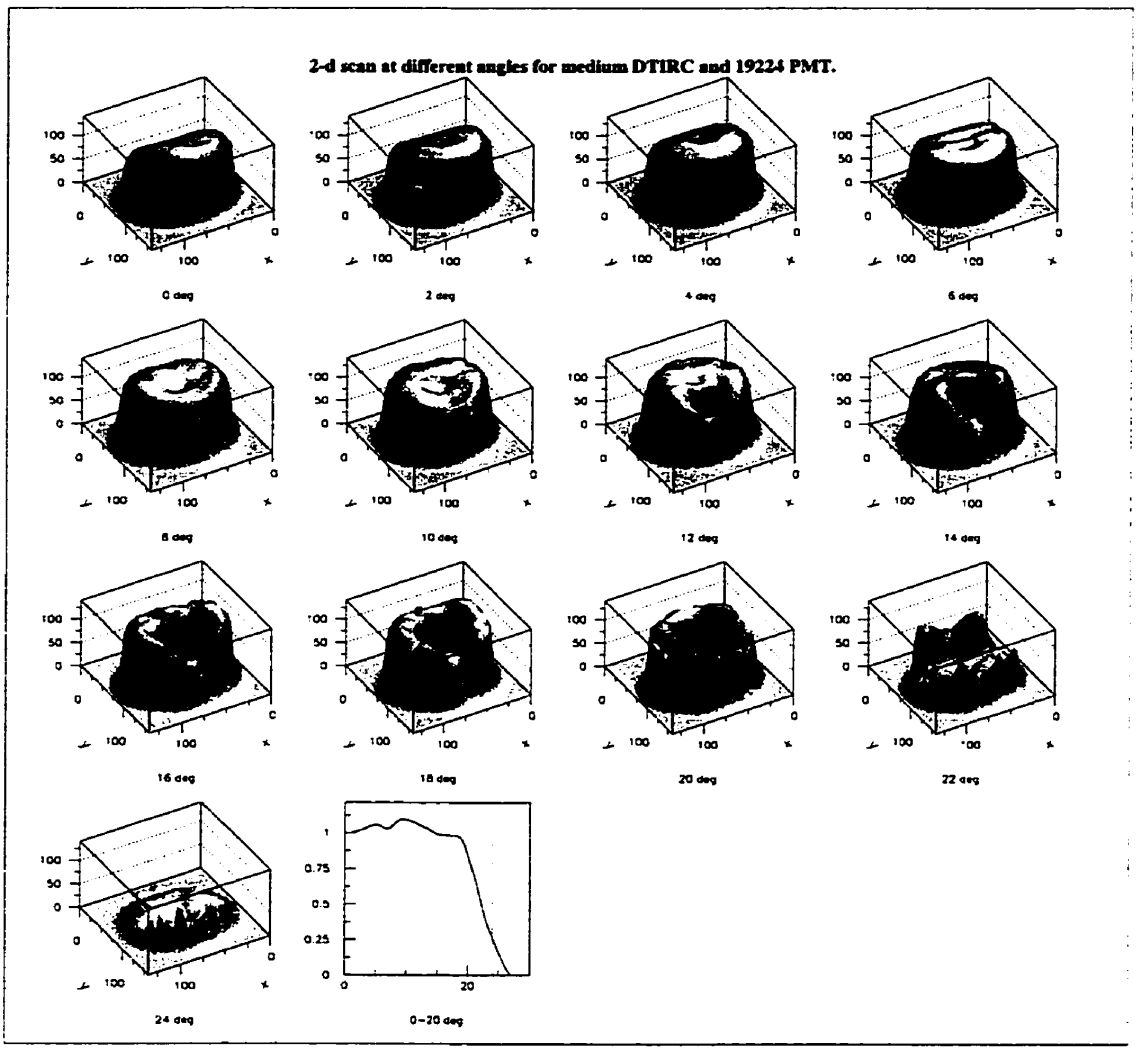

Figure 4.9: Two-dimensional scan of PMT #19224 and a medium DTIRC with a pulsed blue LED. X and Y axis are in mm and the Z axis is the number of ADC counts. The last panel shows the total response of the detector as a function of the angle of incidence (normalized to response at 0°). The dotted line shows the nominal cut-off angle.

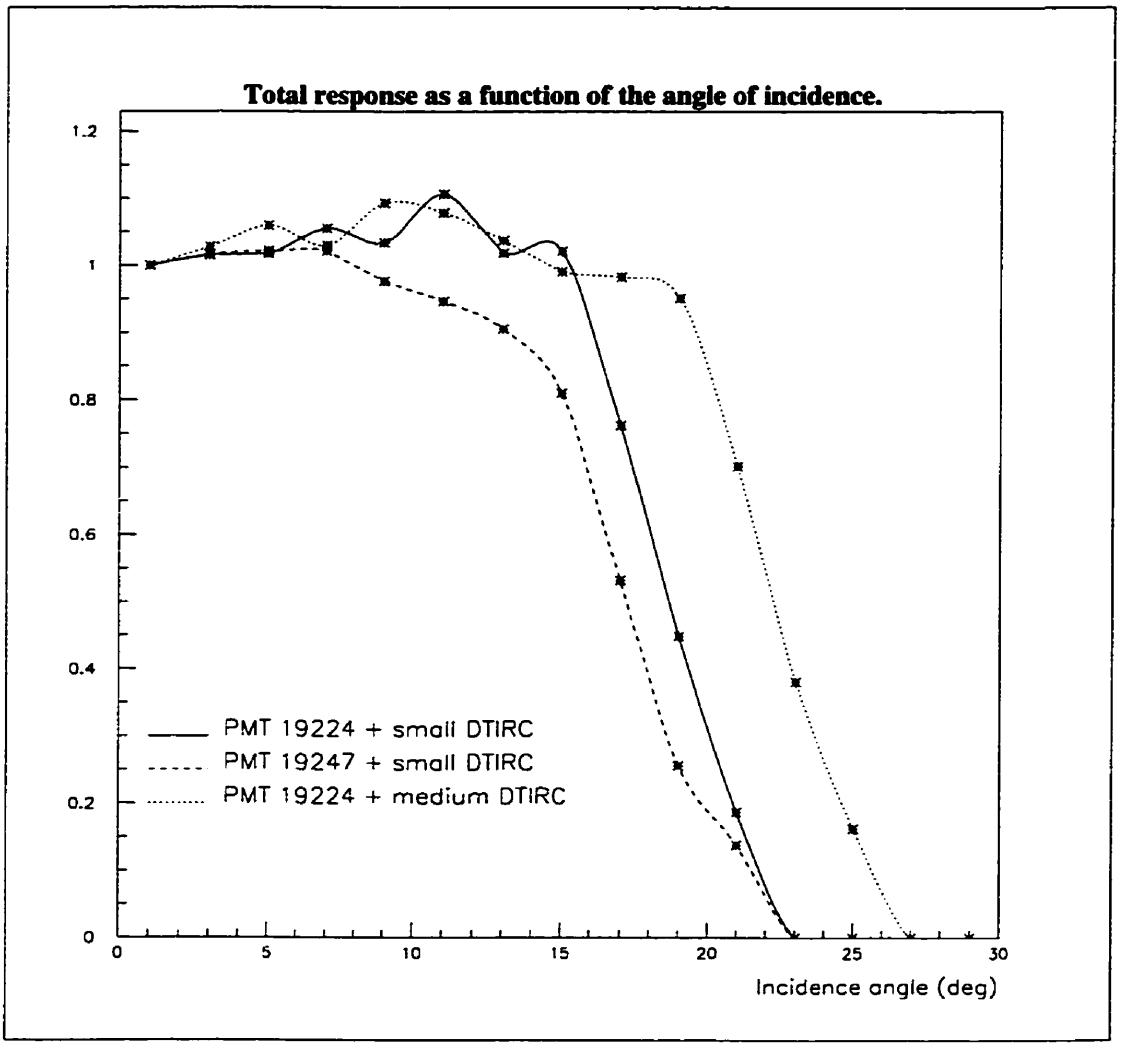

Figure 4.10: Total response of different combinations of PMTs and DTIRCs.

performance and that this can be quantified with our apparatus.

4.2.3 DTIRC versus hollow Winston cone

Optical decoupling of DTIRCs due to thermal expansion of the silicon rubber cookie was a problem encountered early in the STACEE experiment. A possible solution to this problem is to use hollow Winston cones which do not require optical coupling. A hollow Winston cone consists of a cylindrical block of plastic into which the shape of a Winston cone is bored. A thin layer of reflective material is then applied on the inner surface. Our instrument was used to study two models of these hollow Winston cones, and to compare them to DTIRCs. One cone was made of ABS plastic, and the other was made of acrylic. A thin layer of aluminum was used as the reflective medium. We did a two-dimensional scan at 0° with a pulsed blue LED. The result is shown in Figure 4.11. The response of the DTIRC was obviously more uniform than the response of either of the 2 cones. The drops observed in the response of the second cone are due to the fact that the diameter at the base of the cone was larger than the diameter of the photocathode. Nevertheless, even for the first cone the response shows substantial variability. The responses of the hollow Winston cones were disappointing and the STACEE group will probably continue to work with DTIRCs.

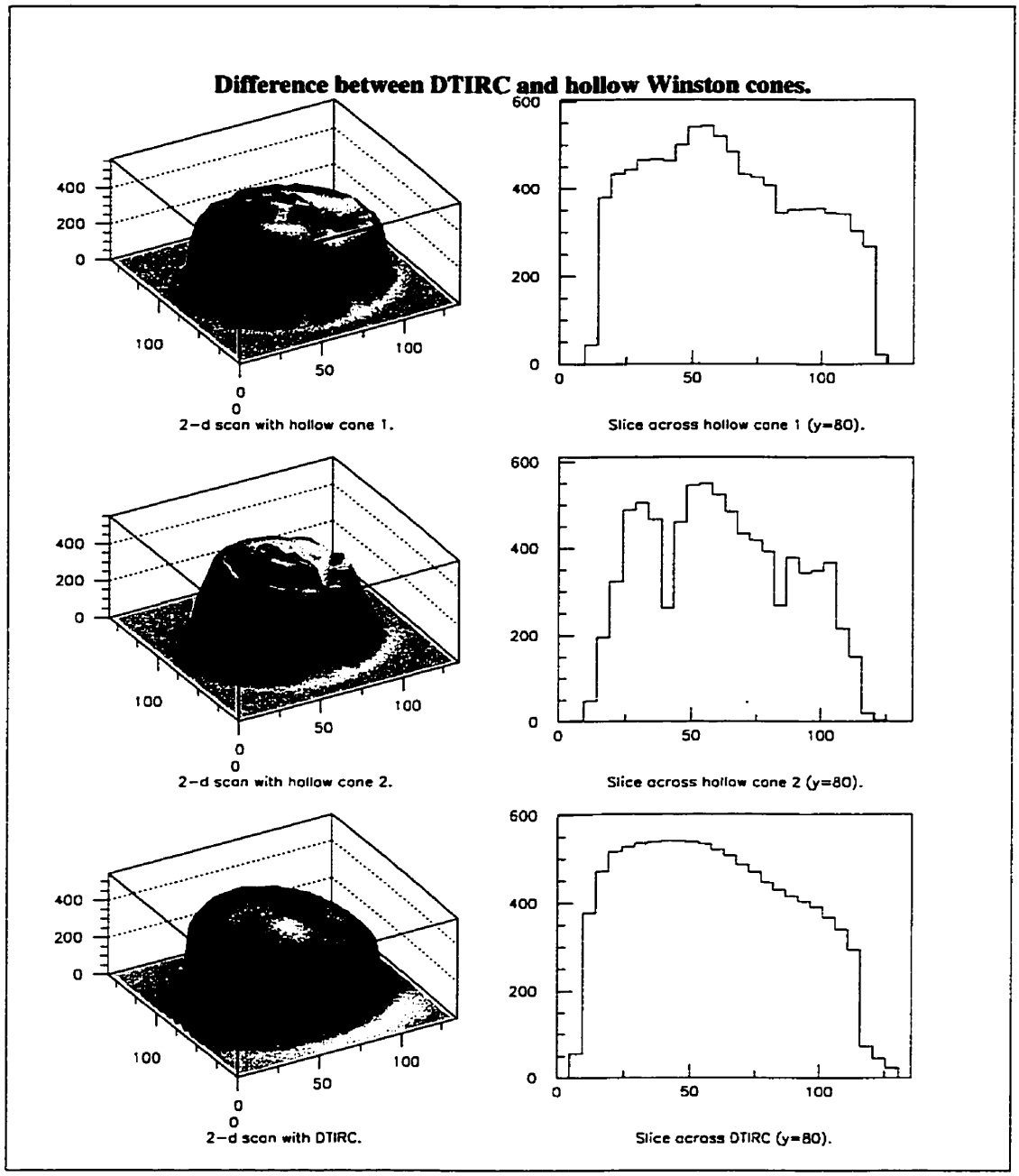

Figure 4.11: Difference between DTIRC and Hollow cones. X and Y axis are in mm and the Z axis is the number of ADC counts.

Chapter 5

Conclusions

The instrument described here is presently being used at McGill University to test all the PMTs of the STACEE experiment. It is anticipated that the results of these tests will be incorporated into a Monte Carlo simulation of the experiment, allowing an improved modelling of the camera response to Cherenkov light. We will eventually rely on this simulation to determine the overall response of the STACEE detector and, hence, the energy of the primary gamma ray.

This instrument provides a controlled environment where we can study different properties of individual modules of the STACEE camera. In this thesis we have shown that:

- The response of the PMTs is strongly dependent on the wavelength of the light source.
- There exists a tube to tube variability in the PMT response.

- There exists a variability in the PMT+DTIRC response.
- The response of hollow Winston cones is different from the response of DTIRCs; the latter being much more efficient.

As the STACEE experiment progresses, questions will arise and the versatility of this instrument will surely help us to answer them.

Bibliography

[1] M. Punch, C.W. Akerlof, M.F. Cawley, M. Chantell, et al. Detection of TeV photons from the active galaxy Markarian 421. *Nature*, 358(6386):477–478, 1992.

[2] D. Petry, S.M. Bradbury, A. Konopelko, J. Fernandez, et al. Detection of VHE gamma-rays from Mkn 421 with the HEGRA Cherenkov telescopes. *Astronomy & Astrophysics*, 311(3):13–16, 1996.

[3] J. Quinn, C.W. Akerlof, S. Biller, J. Buckley, et al. Detection of gamma-rays with energy larger than 300 GeV from Markarian 501. *Astrophysical Journal, Letter*, 456(2):83–86, 1996.

[4] A. Barrau, R. Bazer-Bachi, H. Cabot, L.M. Chounet, et al. Detection of VHE gamma-rays from MRK 501 with the Cat Imaging Telescope. In *Proceedings of the 25th International Cosmic Ray Conference*, page 253, 1997.

[5] Xiaohui Ning, Roland Winston, and Joseph O'Gallagher. Dielectric totally internally reflecting concentrators. *Applied optics*, 26(2):300–305, 1987.

[6] J.A. Soules, D.R. Buchele, C.H. Castle, and R.P. Macosko. Design and fabrication of a dielectric total internal reflecting concentrator and associated flux extractor for extremely high-temperature (2500 k) applications. *Proceedings of Spie - the International Society for Optical Engineering*, 3139:237–249, 1997.

[7] Philips data handbook. *Photo and electron multipliers*, sep 1982.

[8] Philips Photonics. *Photomultiplier tubes, principles and applications*, 1994.